

Energy gaps in the $4f^{13}5d^1$ manifold and multiple spontaneous emissions in Yb^{2+} -doped CsCaBr_3 .

Goar Sánchez-Sanz,¹ Luis Seijo,^{1,2} and Zoila Barandiarán^{1,2,*}

¹*Departamento de Química, C-XIV,*

Universidad Autónoma de Madrid, 28049 Madrid, Spain

²*Instituto Universitario de Ciencia de Materiales Nicolás Cabrera,*

Universidad Autónoma de Madrid, 28049 Madrid, Spain

(Dated: May 14, 2009)

Abstract

Multiple spontaneous $4f^{13}5d^1 \rightarrow 4f^{14}$ emissions are predicted in Yb^{2+} -doped CsCaBr_3 crystals by *ab initio* quantum chemical calculations. Four emission bands are found at 23900, 26600, 34600, and 43900 cm^{-1} that should be experimentally observable at low temperatures. The first, third, and fourth bands are slow, electric dipole forbidden emissions that can be described as spin-forbidden. The second band is a fast, electric dipole allowed emission that cannot be described as spin-allowed, but as spin-enabled; its radiative emission lifetime is 400 *ns*. Large energy gaps (23900, 4600, 4000 cm^{-1} , respectively), relative to the maximum local phonon energies calculated (around 185 cm^{-1}), are found below the emitting levels of the slow bands, which indicates that these states should be significantly stable and multiphonon relaxation to the lower states should be negligible. A smaller gap (2600 cm^{-1}) separates the states of the fast band, which should result in a temperature dependent competition between radiative and non-radiative decay. Differential correlation between $4f-4f$ and $4f-5d$ pairs, splitting of the $5d$ shell by interactions with the host, and spin-orbit effects within the $4f^{13}$ sub-shell, are found to be responsible for the existence of the gaps, which, in turn, split the absorption spectrum into four groups of separate bands, three of which could lie below the host absorption threshold. The quantum chemical methods employed make use of explicit wave functions expanded in terms of flexible basis sets, multiconfigurational self-consistent-field and multireference second-order perturbation methods to account for non-dynamic and dynamic electron correlation, scalar and relativistic terms in the $(\text{YbBr}_6)^{4-}$ defect cluster Hamiltonian, and quantum mechanical embedding potentials to represent the host crystal.

I. INTRODUCTION

Two characteristics of divalent lanthanide ions (Ln^{2+}) in crystals can be pointed out as responsible for the growing number of reports on their optical properties in the last few years (see Ref. 1 for a review; for an overview on recent works see Ref. 2). First, their $4f^N \rightarrow 4f^{N-1}5d^1$ excitations occur at much lower energies than in the isoelectronic trivalent series (Ln^{3+}), in the near-IR, visible, and near-UV. As a consequence of this, large portions of their $4f^{N-1}5d^1$ manifolds are experimentally accessible and a variety of crystals, including crystals of heavy (polarizable) halides, can be chosen as host matrices, in contrast with the wide band gap hosts (commonly fluorides and oxides) typically needed to reach the $4f^{N-1}5d^1$ states in the Ln^{3+} series. Second, and very interesting from practical and basic points of view, the $4f^{N-1}5d^1$ manifolds of the heavy members ($N > 7$) may contain a number of metastable excited states, as deduced from the facts that two emission bands^{2,3} and very unusual multiple spontaneous emissions³⁻⁵ have been detected, and upconversion luminescence has been proven and interpreted in terms of energy transfer mechanisms where more than one $4f^{N-1}5d^1$ states are involved.^{6,7} These spectral features highlight the potentiality of divalent lanthanides in the fields of solid state lasers⁸ and solid state lighting, and show them as very promising phosphors for future technology based in their combination with light-emitting diodes as pump sources.⁶ They also highlight the importance of providing *ab initio* theoretical descriptions to the underlying electronic structures, for which semi-quantitative models and schematic energy diagrams⁹ or empirical crystal field analyses² are often used.

The stability of excited states of rare-earth ions in crystals was already investigated in very early spectroscopic works where it was observed that, if two spin-orbit levels were sufficiently close in energy, the upper level would not be sufficiently stable to fluoresce, a fact that promoted theoretical and experimental approaches to understanding multiphonon relaxation processes and their interplay with radiative processes (see references 10–12 and references therein). As a consequence, a number of factors are now recognized to play an important role in favoring the stability of excited states.¹⁰⁻¹⁴ Among them, a key factor is the existence of large energy gaps in the manifold of excited states, but, also important are the value of the maximum phonon energy of the material and the spin character of the excited states separated by the gaps.¹⁰⁻¹⁴

The progress of solid state quantum chemical methods has made it possible to obtain information about these factors independently from experiments, this being the main characteristic of the so-called *ab initio* methods. The calculation of potential energy surfaces of excited states is a typical target for *ab initio* methods of quantum chemistry based on the explicit use of multiconfigurational wave functions.^{15–17} When these methods are combined with embedding techniques^{18,19} and the Hamiltonians used include scalar and spin-dependent relativistic terms,^{18,20} they can be applied to the calculation of local excited states of *f*-elements in the solid state and to their phosphor properties.^{21–23} From the analyses of the potential energy surfaces and the corresponding wave functions, the energy gaps below excited states can be quantified, the energy of the local vibrational frequencies can be calculated, and the contributions of terms of different spin and spatial symmetries can be traced back from the spin-orbit wave functions. All of these results give the quantum chemical picture of existing empirical data on *f*-element based phosphors or the quantum chemical prediction of their luminescence data not yet available. In any case, the insight gained from the analyses of experiments using semiquantitative models or empirical theories, in these types of materials, is expanded.

In this work we have applied *ab initio* quantum chemical methods to the calculation of the energy gaps in the manifold of excited states of Yb²⁺ doped CsCaBr₃ crystals in order to explore whether multiple spontaneous emissions can be expected in this material. The choice of this particular impurity-host combination also responds to the following reasons: (i) Yb²⁺ is a good candidate among the heavy divalent lanthanides because it has the simplest possible $4f^N$ manifold, formed by its spin-singlet $4f^{14}$ ground state, which focuses the computational effort and analyses on the $4f^{N-1}5d^1$ and $4f^{N-1}6s^1$ excited manifolds, (ii) CsCaBr₃ is a good host because it has been recently shown to favor multiple emissions in heavy Ln²⁺ ions like Tm²⁺,⁴ and it is known that divalent lanthanides can be stabilized in this matrix,^{3,4,7} (iii) as far as we know, no reports on the spectroscopic properties of the CsCaBr₃:Yb²⁺ material exist other than Ref. 3 and, hence, the predictions of the present work should serve to evaluate the interest of and orient future experimental work on this material.

The results of the calculations and their analyses show that differential correlation between $4f$ – $4f$ and $4f$ – $5d$ electron pairs, splitting of the $5d$ shell in the crystal field, and spin-orbit effects in the $4f^{N-1}$ subshell, contribute to the existence of five energy gaps which

determine the structure of the absorption and emission spectra. The absorption spectrum is split in four groups of separate bands of increasing intensity, three of which could lie below the host absorption. The emission spectrum consists of four emission bands at 23900, 26600, 34600, and 43900 cm^{-1} that should be experimentally observable at low temperatures. The second band is a fast, electric dipole allowed emission, whose radiative emission lifetime is 400 ns ; the rest of bands are slow, electric dipole forbidden emissions. Competitive non-radiative decay from the states at 26600 cm^{-1} is also predicted; this should result in temperature dependent non-radiative feeding of the lowest, slow, forbidden band.

II. DETAILS OF THE CALCULATIONS

The quantum chemical methods employed here make use of explicit wave functions expanded in terms of flexible basis sets, multiconfigurational self-consistent-field¹⁵ and multireference second-order perturbation methods^{16,17,24,25} to account for non-dynamic and dynamic electron correlation, scalar and relativistic terms in the $(\text{YbBr}_6)^{4-}$ defect cluster Hamiltonian,^{18,26} and quantum mechanical embedding potentials to represent the host crystal.^{18,27} All the methods used have been described elsewhere; therefore, we only give here the details necessary so that the present calculations are reproducible.

Within the $(\text{YbBr}_6)^{4-}$ octahedral defect cluster, relativistic core *ab initio* model potentials (AIMP) have been used to represent the $[\text{Kr}]$ core of Yb²⁸ and the $[\text{Ar}, 3d]$ cores of Br;²⁹ the corresponding Yb valence basis set $(14s10p10d8f)$,³⁰ supplemented with three g -type functions that give maximum radial overlap with the $4f$ atomic orbital, is contracted as $[6s5p6d4f1g]$; the Br basis set used, $(9s9p4d)[3s5p2d]$, includes three d -type orthogonality functions which give maximum radial overlap with the $3d$ core orbital, one d -type polarization function³¹ and one p -type diffuse function for anions with orbital exponent $\zeta = 0.03681605$.³² We have also used a $(10s7p)/[1s1p]$ basis set at the second neighbour Ca sites to favour strong orthogonality with the environment; the contracted Gaussian functions are the external Ca^{2+} $3s$ and $3p$ embedded atomic orbitals calculated in the procedure followed to produce the AIMP embedding. The $(\text{YbBr}_6)^{4-}$ Hamiltonian includes the AIMP embedding potentials obtained in a previous work³³ to represent the Cs^+ , Ca^{2+} , and Br^- ions located at their cubic crystal structure sites.³⁴ All the ions located within a cube of length $4a_0$, centered at the impurity site, have been represented by AIMPs; point-charges

have been used for the rest of ions located within a cube of length $7a_0$; fractional charges have been assigned to those located at the faces, edges, or corners of the outermost cube, following Evjen’s method.³⁵

Electron correlation and spin-orbit coupling have been combined together following a two-step method. In a first step, spin-orbit terms have been excluded in the embedded cluster Hamiltonian and state-average complete active space self consistent field calculations (SA-CASSCF)¹⁵ have been performed using the scalar terms of the relativistic Wood-Boring AIMP²⁶ Hamiltonian. The active space used results from distributing the 14 open-shell electrons in 13 active molecular orbitals with main character Yb $4f$, $5d$, $6s$, this being the standard choice for a lanthanide.³⁶ These calculations are referred to as CASSCF($4f,5d,6s$) in the next Sections. Dynamic electron correlation has been taken into account using the SA-CASSCF wave functions in subsequent multistate second-order perturbation theory calculations (MS-CASPT2),^{16,17,24,25} where 80 valence electrons occupying the cluster molecular orbitals with main character Br $4s$, $4p$ and Yb $4d$, $5s$, $5p$, $4f$, and $5d/6s$ were correlated; these calculations are referred to as MS-CASPT2(Br48,Yb32). The program MOLCAS has been used for these calculations.³⁷ In a second step, the full Wood-Boring AIMP Hamiltonian,²⁶ which includes the spin-orbit coupling operator (scaled by a factor of 0.9, as proposed in Ref. 38), has been used to perform double-group spin-orbit configuration-interaction (CI) calculations. The shifting operator included in this Hamiltonian, the so-called spin-free-state-shifting (sfss) operator,³⁹ transports the dynamic electron correlation effects retrieved at the spin-orbit free MS-CASPT2(Br48,Yb32) level onto the smaller configurational space used in the spin-orbit CI calculations, which include the restricted active space formed by the $4f^{13}5d^1$ and $4f^{13}6s^1$ multireference plus all single excitations from the $4f$, $5d$, and $6s$ molecular orbitals to the virtual orbitals. For these calculations, the bases described above were truncated to Yb[$6s5p6d4f$], Br[$3s3p$]. We refer to these calculations as SO-CI; they have been done using the COLUMBUS package.⁴⁰ The EPCISO program⁴¹ has been used to calculate electric dipole transition moments. All AIMP data (for embedding and/or for cores) and valence basis sets can be found in Ref. 42.

III. RESULTS AND DISCUSSION

We discuss here the results of the quantum chemical investigation of the absorption and luminescence properties of $\text{CsCaBr}_3\text{:Yb}^{2+}$. In a first Subsection, the calculated electronic structure of the $4f^{13}5d^1$ and $4f^{13}6s^1$ states is described in detail and the origin of the energy gaps found in these manifolds is revealed. The structure of the absorption spectrum of $\text{CsCaBr}_3\text{:Yb}^{2+}$ in separated groups of bands and their relative intensities are discussed in a second Subsection. In a third Subsection, a prediction is made, from theory alone, of which excited states should be stable enough to luminesce. Finally, in the last Subsection the results of the calculation are confronted with available experimental information.

A. Structure of the $4f^{13}5d^1$ and $4f^{13}6s^1$ manifolds. Origin of the energy gaps.

The results of the calculations performed in the $(\text{YbBr}_6)^{4-}$ defect cluster, embedded in the CsCaBr_3 host, using the methods described in Section II are presented in Tables I and II, and Figures 1 and 2. They include the $4f^{14}$ ground state and the electronic states showing main configurational character $4f^{13}5d^1$ and $4f^{13}6s^1$.

The potential energy surfaces of all the states mentioned have been calculated firstly at the CASSCF($4f,5d,6s$) level described in Section II. Even though we refer to these states using simple labels corresponding to their main configuration, as above, the calculations are done in a space of about 10^5 configurations. Bonding interactions are only partially described, due to lack of dynamic correlation, nevertheless, the effects of the ligands and of the CsCaBr_3 host, modelled by the quantum mechanical AIMP embedding, are already visible and are responsible for the first energy gap observed, which splits the $4f^{13}5d^1$ manifold in two submanifolds, which can be called $4f^{13}5d(t_{2g})^1$ and $4f^{13}5d(e_g)^1$, and are formed, each, by parallel curves sharing bond distance and a_{1g} vibrational frequency values. (A detailed study of the $4f^{13}5d(t_{2g})^1$ manifold can be found in Ref. 33; for this reason, Tables I and II include only the data that are needed for this paper.) Whereas the bond lengths are shorter in the $4f^{13}5d(t_{2g})^1$ manifold than in the ground state, the opposite is true for the $4f^{13}5d(e_g)^1$ states. These bond length differences have been observed before in f -element doped solids and have been analysed in detail elsewhere.^{43,44} All of these results show the much larger exposure of the $5d$ shell than the $4f$ shell to bonding and host interactions. The energy of

the totally symmetric vibrational frequency, $\bar{\nu}_{a_{1g}}$, is basically the same for all states, at this level of calculation, regardless of their main configurational character.

As soon as dynamic correlation of all valence electrons is treated, using the MS-CASPT2 method referred in Section II, the near degeneracy between the $4f^{14}$ and $4f^{13}5d(t_{2g})^1$ shells is lifted and a large energy gap which separates the ground state from the first excited state is created (see Fig. 1, right and Table I). Dynamic correlation is found to increase the $4f^{13}-4f^{13}5d(t_{2g})^1$ and $4f^{13}-4f^{13}5d(e_g)^1$ energy differences by some 25000 and 27000 cm^{-1} , respectively, in average, as it can be seen in Table I. The large transition energy corrections can be associated with the fact that electron correlation is much larger for tight $4f-4f$ electron pairs than for more distant $4f-5d$ electron pairs and the number of $4f-4f$ pairs substituted by $4f-5d$ pairs is largest in this 14 f -electron system. Electron correlation is found to decrease all bond lengths significantly, by about 0.09–0.10 Å, the reduction being quite uniform; the $\bar{\nu}_{a_{1g}}$ values are only slightly decreased.

Once scalar relativistic effects and dynamic electron correlation have been accounted for at the MS-CASPT2 level, it is possible to include spin-orbit coupling by doing spin-orbit CI calculations using the *sfss* Wood-Boring AIMP Hamiltonian, as described in Section II. The effects of spin-orbit coupling become evident if the calculated potential energy surfaces of the $4f^{13}5d(t_{2g})^1$, $4f^{13}5d(e_g)^1$ and $4f^{13}6s^1$ manifolds in Figure 2 are compared (see also Tables I and II). New energy gaps are created which split the $4f^{13}5d(t_{2g})^1$, $4f^{13}5d(e_g)^1$ and $4f^{13}6s^1$ manifolds into two submanifolds each, which, using free ion language, correspond to the coupling of the $4f^{13}(J=7/2)$ and $4f^{13}(J=5/2)$ subshell components with the $5d(t_{2g})^1$, $5d(e_g)^1$, and $6s^1$ electron, respectively. Due to the proximity in energy of the $4f^{13}5d(e_g)^1$ and $4f^{13}6s^1$ manifolds, at the spin-orbit free level, on the one hand, and the magnitude of the $4f^{13}(7/2)$ and $4f^{13}(5/2)$ splitting, on the other hand (see below), the $4f^{13}(5/2)5d(e_g)^1$ and $4f^{13}(7/2)6s^1$ submanifolds overlap in energy and significant $4f^{13}5d(e_g)^1$ and $4f^{13}6s^1$ configuration interaction occurs between them. Since their average bond lengths are different ($\langle R_e[4f^{13}5d(e_g)^1] \rangle = 2.74 \text{ Å}$, $\langle R_e[4f^{13}6s^1] \rangle = 2.82 \text{ Å}$) the configurational mixing results in very distorted potential energy surfaces with intermediate bond length values (see Table II). The spin-orbit splitting of the $4f^{13}$ subshell can be estimated from the difference in the average energies of the $4f^{13}(5/2)5d(t_{2g})^1$ (38100 cm^{-1}) and $4f^{13}(7/2)5d(t_{2g})^1$ (27600 cm^{-1}) states, which is about 10500 cm^{-1} (Figure 2, right), or as the energy difference from the lowest states which keep $4f^{13}(5/2)5d(e_g)^1$ character and the lowest states of the $4f^{13}(7/2)5d(e_g)^1$

manifold, i.e., $T_e(6A_{1u}) - T_e(8E_u) = 10000 \text{ cm}^{-1}$ (Table II). These differences are close to the corresponding value in the free ion: 10800 cm^{-1} .⁴⁵

A much smaller energy gap is found in the lower energy part of the $4f^{13}(7/2)5d(t_{2g})^1$ manifold, between states $1T_{2u}$ and $1T_{1u}$, (see Figure 2, right). This energy gap has been discussed in detail in Ref. 33, where it has been shown to be a consequence of the energy separation between the lowest high-spin state, 1^3T_{1u} , and the next higher $4f^{13}5d(t_{2g})^1$ state, as calculated at the spin-orbit free MS-CASPT2 level (see Figure 2, left).

B. The absorption spectrum of Yb^{2+} -doped CsCaBr_3 .

The envelope of the absorption spectrum presented in Fig. 3 was produced as a superposition of the a_{1g} vibrational progression of each individual electric dipole allowed transitions $4f^{14-1} A_{1g} \rightarrow i T_{1u}$ ($i = 1, 21$) calculated using the semiclassical time-dependent approach of Heller with different values for the line broadening parameter (40 and 5 cm^{-1} in the low and high resolution spectra, respectively).⁴⁶⁻⁴⁸ To do this, the calculated equilibrium distance and a_{1g} vibrational frequencies of the ground and excited states were used together with the corresponding minimum-to-minimum energy differences and absorption oscillator strengths (Table II). Some electric dipole forbidden transitions that should be experimentally observable as low intensity vibronic transitions preceding the intense electric dipole allowed bands have been indicated with vertical bars.

The calculated spectrum consists of 4 separated groups of bands (Fig. 3). This structure is consistent with the existence of manifolds and submanifolds, separated by energy gaps, we have just discussed in Subsection III A. The electronic origins with non-negligible absorption oscillator strengths that contribute to each group and their assignment to manifolds with a dominant configuration character are as follows: Group 1 is formed by origins $i = 1, 2, 5$, and 6 of manifold $4f^{13}(7/2)5d(t_{2g})^1$; group 2, by origins $i = 7, 8$, and 10 of manifold $4f^{13}(5/2)5d(t_{2g})^1$; group 3, by origins $i = 12 - 15$ of manifold $4f^{13}(7/2)5d(e_g)^1$; and group 4, by origins $i = 16, 17$, and 18 , of which, origin $16T_{1u}$ has dominant $4f^{13}(5/2)5d(e_g)^1$ character, whereas $17T_{1u}$ and $18T_{1u}$ have increasing $4f^{13}6s^1$ contribution. In this way, whereas the crystal field effects on the $5d$ electron are responsible for the energy difference between groups 1 and 3, on the one hand, and 2 and 4, on the other hand, the spin-orbit splitting of the $4f^{13}$ subshell is responsible for the energy difference between groups 1 and 2 and, also,

between groups 3 and 4.

The intensity of excitations to $4f^{13}5d(t_{2g})^1$ states (groups 1 and 2) are significantly smaller than the intensity of excitations to $4f^{13}5d(e_g)^1$ states (groups 3 and 4), by a factor of 3–4, as it can be observed in Fig. 3. This feature is related with atomic selection rules, as we comment next. On the one hand, the results presented in the previous Subsection (Fig. 2, Table II) indicate that the 1, 2, and 3 $^1T_{1u}$ enabling terms of the spin-orbit free calculation contribute to the T_{1u} states of $4f^{13}5d(t_{2g})^1$ character, whereas the terms 4 and 5 $^1T_{1u}$ contribute to those of $4f^{13}5d(e_g)^1$ character. Furthermore, the calculated squares of the electric dipole transition moment, μ^2 , of pure spin-orbit free $1^1A_{1g} \rightarrow i^1T_{1u}$ transitions, are: 0.010, 0.186, 0.510, for $i=1,2,3$, and 0.007 and 1.281, for $i=4,5$, which is consistent with the observation in Fig. 3. On the other hand, Yb^{2+} free ion calculations performed by us using the same levels of methodology, reveal that the energy order of atomic $4f^{13}5d^1$ $2S+1=1$ terms leading to $^1T_{1u}$ crystal wave functions is as follows: $^1H < ^1G < ^1F < ^1P$, which makes it reasonable to expect that the only electric dipole enabling character, 1P , is maximum for the highest $4f^{13}5d^1$ crystal term, 5^1T_{1u} , which, in turn, is consistent with the large value of $\mu^2(1^1A_{1g} \rightarrow 5^1T_{1u})$ and the observed higher intensity of excitations to $4f^{13}5d(e_g)^1$ states.

The vibrational progressions of the origins associated with the $4f^{13}5d(t_{2g})^1$, $4f^{13}5d(e_g)^1$, and $4f^{13}6s^1$ manifolds are also different and consistent with the absolute value of the offset of their characteristic bond length. The bond length differences relative to the ground state are: $\Delta R_e[4f^{13}5d(t_{2g})^1] = -0.029 \text{ \AA}$, $\Delta R_e[4f^{13}5d(e_g)^1] = +0.011 \text{ \AA}$, $\Delta R_e[4f^{13}6s^1] = +0.086 \text{ \AA}$, at the MS-CASPT2 level (Table I), and spin-orbit interaction changes these values only in the manifold of higher energy, where $4f^{13}5d(e_g)^1$, $4f^{13}6s^1$ interaction occurs leading to intermediate values of equilibrium distances and offsets between $+0.011$ and $+0.086 \text{ \AA}$. Hence, the vibrational progression intensities are as follows (see Fig. 3 and confront individual equilibrium geometries in Table II): For origins 1 to 10, of $4f^{13}5d(t_{2g})^1$ character, the 0-0 and 0-1 lines have very similar and maximal intensity, and the progression includes up to the 0-3 member. For origins 12 to 15, of $4f^{13}5d(e_g)^1$ character, the 0-0 line dominates the progression, which also includes, with much smaller intensity, the 0-1 member. Finally, the progressions of origins 16 to 18 show the effects of increasing mixing of $4f^{13}5d(e_g)^1$ with $4f^{13}6s^1$ configurations. So, the maximum intensity line moves from being the 0-0 (for origin 16) to the 0-3 (origin 17) to the 0-6 (for origin 18). Also, as the $4f^{13}6s^1$ character becomes important (origin 18) the atomic selection rule that forbids $f \leftrightarrow s$ transitions becomes

apparent in the lower absorption oscillator strength value.

The fact that the $4f^{13}6s^1$ states are so high in energy in the crystal, whereas they are among the lowest excited states in the free ion, is an interesting feature. The question of why these states are destabilized so strongly in the solid is discussed elsewhere.³³

C. Multiple spontaneous emissions in $\text{CsCaBr}_3:\text{Yb}^{2+}$.

In Table III we collect the data corresponding to the potentially emitting levels. They lie immediately above the five energy gaps we have just discussed and all but the highest in energy, which is probably in the conduction band (CB), should be stable enough to luminesce. To support this conclusion, we have estimated the approximate order, p , of the multiphonon process that could compete with the radiative emission from each level $i\Gamma$, as proposed in Ref. 10: $p = E_{\text{gap}}(i\Gamma)/\hbar\nu_{\text{max}}$ (see Table III). For this, we have used the energy gap below state $i\Gamma$, $E_{\text{gap}}(i\Gamma)$, and the $\bar{\nu}_{a_{1g}}$ value of the level lying below the gap as maximum phonon frequency, ν_{max} (Table II). The values of p make it reasonable to expect that multiphonon relaxation processes could be competitive in the case of $1T_{1u}$ state and negligible for the rest of states. The different spin character of the states lying above and below the gap also supports their stability, as revealed by the term analysis of the wave functions. Whereas the states lying above the large energy gaps, $1T_{2u}(90\%1^3T_{1u})$ and $1E_u(90\%1^3T_{1u})$, $3A_{1u}(94\%1^3T_{1u})$, $8E_u(88\%4^3T_{1u})$, and $6A_{1u}(97\%4^3T_{1u})$, can be classified as high-spin states, since their spin-orbit wave functions are dominated by a particular high-spin term of T_{1u} spatial symmetry whose contribution is larger than 85%, the states lying below the large energy gaps show extensive spin-orbit mixing and cannot be classified as high-spin states nor as low-spin states, but as spin-mixed states. The opposite is true for the states lying above and below the smaller energy gap: whereas $1T_{1u}$ and $2T_{1u}$ (see Table II), are spin-mixed states, $1T_{2u}$ and $1E_u$ are 90% high-spin 1^3T_{1u} .

The characteristics of the predicted spontaneous emissions are summarized in Table III; the two lowest emission bands are also presented in Fig. 4. The first band is a double emission that corresponds to the $1T_{2u}, 1E_u \rightarrow 1A_{1g}$ electric dipole forbidden transitions and is indicated with vertical bars in Fig. 4. As mentioned above it can be labeled as a spin-forbidden band and it should lead to a slow emission. The second band is an electric dipole allowed double emission and its envelope has been calculated as a superposition of the a_{1g}

vibrational progression of the individual electric dipole allowed transitions $1T_{1u}$, $2T_{1u} \rightarrow 1A_{1g}$ using the semiclassical time-dependent approach of Heller.^{46–48} Their emission oscillator strengths [$f(1T_{1u} \rightarrow 1A_{1g}) = -0.273 \times 10^{-2}$, $f(2T_{1u} \rightarrow 1A_{1g}) = -1.260 \times 10^{-2}$] and spectroscopic data in Table II have been used for that purpose, and thermal equilibrium among $1T_{1u}$ and $2T_{1u}$ has been assumed, so that the contribution of the progression of the latter has been scaled by the corresponding Boltzmann factor (0.45 for $T = 77$ K). As commented above, the emitting states in this band are spin-mixed and this band drives its intensity from no other terms than the enabling low-spin $1T_{1u}$ states which contribute to their spin-orbit wave functions; for this reason, this band has been called “spin-enabled” in Ref. 33, where a detailed study of the differences in the electronic structure of the low lying excited states of $\text{CsCaBr}_3:\text{Yb}^{2+}$ has been presented. The spontaneous emission from these states should be significantly faster. The calculated emission lifetimes of $1T_{1u}$ and $2T_{1u}$ are respectively 1100 and 150 *ns*; when thermal equilibrium is considered, the band emission lifetime becomes 400 *ns*. Finally, the third and fourth emission bands, corresponding to $3A_{1u} \rightarrow 1A_{1g}$ and $8E_u \rightarrow 1A_{1g}$, respectively, are also electric dipole forbidden, spin-forbidden, slow emissions, as indicated in Table III.

D. Theory and experiment.

Heavy Ln^{3+} and Ln^{2+} ions in crystals share the following interesting spectral features: (representative references are 2,4,9,14,49): (i) A weak band is present in their f – d absorption and/or excitation spectra at lower energies than the strong f – d bands. (ii) A slow d – f emission band is observed in their luminescence spectra at lower energies than a fast d – f emission band (the emissions referred to are to the $4f^N$ ground state). (iii) Strong temperature dependence of the relative intensities of these emissions has been reported and it has been interpreted as a manifestation of competing radiative and nonradiative decay from the higher state, which favours nonradiative feeding of the lower state as the rate of the non-radiative process increases with temperature, so that a gradual change of relative intensities is observed from the low T limit, where the intensity of the higher, fast emission is largest, to the high T limit, where the intensity of the lower, slow emission is largest.

The first two bands of the calculated absorption and emission spectra of $\text{CsCaBr}_3:\text{Yb}^{2+}$, presented here, agree with (i) and (ii), respectively. The prediction that non-radiative decay

from $1T_{1u}$ and $2T_{1u}$ to $1T_{2u}$ and $1E_u$ should be competitive with radiative decay, discussed above, is also in agreement with (iii). However, the methods used here do not allow to calculate non-radiative relaxation rates and, hence, the temperature dependence of the relative intensity of the first two emission bands cannot be calculated; furthermore, the spontaneous emission lifetime calculated here refers only to the radiative process (which, nevertheless, is useful to infer the contribution of the non-radiative process to the experimental emission lifetime). Taking all of the latter into account, the calculated emission lifetime and emission spectrum in Fig. 4 should be comparable with the low T emission lifetime and emission spectrum. As far as we know, the only report on the spectral features of $\text{CsCaBr}_3\text{:Yb}^{2+}$ crystals is that of Ref. 3. The 77 and 300 K emission spectra were presented in the range of 21000 to 25800 cm^{-1} . Both spectra show two very broad, structureless bands whose relative intensities vary with temperature as we have just described. The peak positions at 77 K seem to be at 23000 and 24500 cm^{-1} , the intensity of the lower band is almost negligible, and no report on emission lifetime values was given. Our results agree with the intensity pattern, deviate 900 and 2100 cm^{-1} from the peak positions (Table III), give a 20% narrower higher band, and a too large (by 900 cm^{-1} , 50%) gap between the two bands.

The comparison with the data reported in Ref. 3 is, however, very uncertain and more experimental work is necessary which explores lower temperatures and emission lifetimes, and, very important, which extends the investigation of the emission spectrum to much higher energies, given the predictions of this paper on multiple luminescence.

IV. CONCLUSIONS

Multiple spontaneous $4f^{13}5d^1 \rightarrow 4f^{14}$ emissions are predicted in Yb^{2+} -doped CsCaBr_3 crystals by *ab initio* quantum chemical calculations. Four emission bands are found at 23900, 26600, 34600, and 43900 cm^{-1} that should be experimentally observable at low temperatures. They are assigned to emissions from the following electronic states, respectively: $4f^{13}(7/2)5d(t_{2g})^1-1T_{2u}$, $1E_u$; $4f^{13}(7/2)5d(t_{2g})^1-1T_{1u}$, $2T_{1u}$; $4f^{13}(5/2)5d(t_{2g})^1-3A_{1u}$; and $4f^{13}(7/2)5d(e_g)^1-8E_u$. The first, third, and fourth bands are slow, electric dipole forbidden emissions, which can be described as spin-forbidden given that the corresponding spin-orbit wave functions are dominated (88–97%) by a single term of $^3T_{1u}$ symmetry. The second band is a fast, electric dipole allowed emission that cannot be described as spin-

allowed, because it is an extensive mixture of terms; rather, it can be described as spin-enabled, because it gets its intensity from the contributions of $^1T_{1u}$ enabling terms; its spontaneous (radiative) emission lifetime is 400 *ns*. Large energy gaps are found below the emitting levels of the slow bands (23900, 4600, 4000 cm^{-1} , respectively), relative to the maximum local phonon energies calculated (around 185 cm^{-1}), which indicates that these states should be significantly stable and multiphonon relaxation to the lower states should be negligible. A smaller gap is found below the states of the fast band (2600 cm^{-1}), which should result in a temperature dependent competition between radiative and multiphonon decay. Differential correlation between $4f-4f$ and $4f-5d$ pairs (which increases the energy differences by 25000 – 27000 cm^{-1}), splitting of the $5d$ shell by interactions with the host (around 19000 – 20000 cm^{-1}), and spin-orbit effects within the $4f^{13}$ sub-shell (which is found to be about 10500 cm^{-1}), contribute to the existence of five energy gaps in the $4f^{13}5d^1$ and $4f^{13}6s^1$ manifolds which split the absorption spectrum into four groups of separate bands, three of which could lie below the host absorption, and are the bases for the predicted multiple emissions. The quantum chemical methods employed make use of explicit wave functions expanded in terms of flexible basis sets (of triple- ζ plus polarization quality, plus diffuse functions for anions), multireference spaces and multireference second-order perturbation methods (MS-CASPT2) to account for non-dynamic and dynamic correlation, scalar and relativistic terms in the $(\text{YbBr}_6)^{4-}$ cluster Hamiltonian (spin-free-state-shifting Wood-Boring AIMP), and quantum mechanical embedding potentials (AIMP embedding) to represent the host crystal. Typical discrepancies with experimental transition energies obtained in previous applications to similar systems using the same combination of methods make it reasonable to expect overestimations lower than 10 %; this suggests that the predicted transition energies could be observed experimentally some 2000–3000 cm^{-1} below the predicted values.

V. ACKNOWLEDGEMENTS

This research was supported in part by Ministerio de Ciencia e Innovación, Spain, under contracts CTQ2005-08550 and MAT2008-05379. G.S-S. acknowledges an FPI fellowship

from Ministerio de Ciencia e Innovación, Spain.

* Corresponding author; Electronic address: zoila.barandiaran@uam.es

- ¹ J. Rubio, J. Phys. Chem. Solids **52**, 101 (1991).
- ² Z. Pan, C. Duan, and P. A. Tanner, Phys. Rev. B **77**, 085114 (2008).
- ³ P. Larsen, M. Adlung, and C. Wickleder, Rare Earth Conference, Wroclaw, 2006 (unpublished), Abstract CI3.
- ⁴ J. Grimm and H. U. Güdel, Chem. Phys. Lett. **404**, 40 (2005).
- ⁵ J. Grimm, O. S. Wenger, K. W. Krämer and H. U. Güdel, J. Lumin. **126**, 590 (2007).
- ⁶ E. Beurer, J. Grimm, P. Gerner and H. U. Güdel, J. Amer. Chem. Soc. **128**, 3110 (2006).
- ⁷ J. Grimm, E. Beurer, P. Gerner and H. U. Güdel, Chem. Eur. J. **13**, 1152 (2007).
- ⁸ S. Kück, Appl. Phys. B **72**, 515 (2001).
- ⁹ J. Grimm, E. Beurer, and H. U. Güdel, Inorg. Chem. **45**, 10905 (2006).
- ¹⁰ L. A. Riseberg and H. W. Moos, Phys. Rev. **174**, 429 (1968).
- ¹¹ H. W. Moos, J. Lumin. **1,2**, 106 (1970).
- ¹² C. W. Struck and W. H. Fonger, J. Lumin. **10**, 1 (1975).
- ¹³ C. Reber and H. U. Güdel, J. Lumin. **47**, 7 (1990).
- ¹⁴ R. T. Wegh and A. Meijerink, Phys. Rev. B **60**, 10820 (1999).
- ¹⁵ B. O. Roos, P. R. Taylor, and P. E. M. Siegbahn, Chem. Phys. **48**, 157 (1980); P. E. M. Siegbahn, A. Heiberg, J. Almlöf, and B. O. Roos, J. Chem. Phys. **74**, 2384 (1981); P. Siegbahn, A. Heiberg, B. Roos, and B. Levy, Phys. Scr. **21**, 323 (1980).
- ¹⁶ K. Andersson, P.-Å. Malmqvist, B. O. Roos, A. J. Sadlej, and K. Wolinski, J. Phys. Chem. **94**, 5483 (1990).
- ¹⁷ K. Andersson, P.-Å. Malmqvist and B. O. Roos, J. Chem. Phys. **96**, 1218 (1992).
- ¹⁸ L. Seijo and Z. Barandiarán, in *Computational Chemistry: Reviews of Current Trends*, edited by J. Leszczyński (World Scientific, Singapore, 1999), vol. 4, p. 55.
- ¹⁹ P. Huang and E. A. Carter, Ann. Rev. Phys. Chem. **59**, 261 (2008).
- ²⁰ L. Seijo and Z. Barandiarán, in *Relativistic Electronic Structure Theory: Part 2. Applications*, edited by P. Schwerdtfeger (Elsevier, Amsterdam, 2004), pp. 417–475.
- ²¹ P. A. Tanner, C. S. K. Mak, N. M. Edelstein, K. M. Murdoch, G. Liu, J. Huang, L. Seijo, , and

- Z. Barandiarán, J. Amer. Chem. Soc. **125**, 13225 (2003).
- ²² F. Ruipérez, L. Seijo, and Z. Barandiarán, J. Chem. Phys. **122**, 234507 (2005).
- ²³ J. Gracia, L. Seijo, Z. Barandiarán, D. Curulla, H. Niemansverdriet, and W. van Gennip, J. Lumin. **128**, 1248 (2008).
- ²⁴ A. Zaitsevskii and J. P. Malrieu, Chem. Phys. Lett. **233**, 597 (1995).
- ²⁵ J. Finley, P.-Å. Malmqvist, B. O. Roos and L. Serrano-Andrés, Chem. Phys. Lett. **288**, 299 (1998).
- ²⁶ L. Seijo, J. Chem. Phys. **102**, 8078 (1995).
- ²⁷ Z. Barandiarán and L. Seijo, J. Chem. Phys. **89**, 5739 (1988).
- ²⁸ L. Seijo, Z. Barandiarán, and B. Ordejón, Mol. Phys. **101**, 73 (2003).
- ²⁹ Z. Barandiarán and L. Seijo, Can. J. Chem. **70**, 409 (1992).
- ³⁰ L. Seijo, Z. Barandiarán, and E. Harguindey, J. Chem. Phys. **114**, 118 (2001).
- ³¹ J. Andzelm, M. Klobukowski, E. Radzio-Andzelm, Y. Sakai, and H. Tatewaki, *Gaussian Basis Sets for Molecular Calculations*, edited by S. Huzinaga, (Elsevier, Amsterdam, 1984).
- ³² From B. Roos unpublished ANO-RCC basis set for Br included in the MOLCAS basis set libraries.
- ³³ G. Sánchez-Sanz, L. Seijo, and Z. Barandiarán, in preparation.
- ³⁴ H. J. Seifert and D. Haberhauer, Z. Anorg. Allg. Chem. **491**, 301 (1982).
- ³⁵ H. M. Evjen, Phys. Rev. **39**, 675 (1932).
- ³⁶ L. Seijo and Z. Barandiarán, J. Chem. Phys. **118**, 5335 (2003).
- ³⁷ G. Karlström, R. Lindh, P. A. Malmqvist, B. O. Roos, U. Ryde, V. Veryazov, P. O. Widmark, M. Cossi, B. Schimmelpfennig, P. Neogady, and L. Seijo, Comput. Mater. Sci. **28**, 22 (2003).
- ³⁸ Z. Barandiarán and L. Seijo, J. Chem. Phys. **118**, 7439 (2003).
- ³⁹ R. Llusar, M. Casarrubios, Z. Barandiarán, and L. Seijo, J. Chem. Phys. **105**, 5321 (1996).
- ⁴⁰ COLUMBUS suite of programs. (ARGOS, CNVRT, SCFPQ, LSTRN, CGDBG, and CIDBG.) R. M. Pitzer (principal author). See: A. H. H. Chang and R. M. Pitzer, J. Am. Chem. Soc. **111**, 2500 (1989), and references therein for a description. CNVRT and LSTRN have been adapted to handle AIMP integrals by L. Seijo. CIDBG has been modified for spin-free-state-shifted spin-orbit CI calculations by M. Casarrubios.
- ⁴¹ V. Vallet, L. Maron, C. Teichtel, and J.-P. Flament, J. Chem. Phys. **113**, 1391 (2000).
- ⁴² Detailed core and embedding AIMP data libraries in electronic format are available from

the authors upon request or directly at the address <http://www.uam.es/quimica/aimp/Data/-AIMPLibs.html>. See also Ref. 37.

- ⁴³ Z. Barandiarán and L. Seijo, J. Chem. Phys. **119**, 3785 (2003).
- ⁴⁴ Z. Barandiarán, N. M. Edelstein, B. Ordejón, F. Ruipérez, and L. Seijo, J. Solid State Chem. **178**, 464 (2005).
- ⁴⁵ B. W. Bryant, J. Opt. Soc. Amer. **55**, 771 (1965).
- ⁴⁶ E. J. Heller, J. Chem. Phys. **62**, 1544 (1975).
- ⁴⁷ E. J. Heller, Acc. Chem. Res. **14**, 368 (1981).
- ⁴⁸ J. I. Zink and K. S. Shin, *Molecular distortions in excited electronic states determined from electronic and resonance raman spectroscopy* (Wiley, New York, 1991), vol. 16 of *Advances in Photochemistry*, pp. 119–214.
- ⁴⁹ L. van Pieterse, M. F. Reid, G. W. Burdick and A. Meijerink, Phys. Rev. B **65**, 045114 (2002).

TABLE I: Results of the calculations on the $(\text{YbBr}_6)^{4-}$ cluster that include CsCaBr₃ embedding, 80 valence electron correlation, and scalar relativistic effects. Yb–Br bond distances, R_e , in Å; totally symmetric vibrational frequencies, $\bar{\nu}_{a_{1g}}$, in cm^{-1} ; and minimum-to-minimum energy differences, T_e , relative to the $4f^{14}-1^1A_{1g}$ ground state, in cm^{-1} . Data for the eighteen states in the $4f^{13}5d(t_{2g})^1$ manifold are given in Ref. 33; only those for the two lowest and the highest states are given here. Manifold averages and mean square deviations of the individual values with respect to the averages are labeled as $\langle 4f^{13}5d(t_{2g})^1 \rangle$, $\langle 4f^{13}5d(e_g)^1 \rangle$, and $\langle 4f^{13}6s^1 \rangle$.

state	CASSCF($4f,5d,6s$)			MS-CASPT2(Br48,Yb32)		
	R_e	$\bar{\nu}_{a_{1g}}$	T_e	R_e	$\bar{\nu}_{a_{1g}}$	T_e
1 $^1A_{1g}$	2.820	192	0	2.732	184	0
$\langle 4f^{13}5d(t_{2g})^1 \rangle$	2.796 ± 0.001	192 ± 1		2.703 ± 0.002	187 ± 1	
1 $^3T_{1u}$	2.799	193	2302	2.708	185	28406
2 $^3T_{1u}$	2.797	192	5637	2.705	188	31098
2 $^1T_{2u}$	2.795	192	9910	2.703	187	34901
$\langle 4f^{13}5d(e_g)^1 \rangle$	2.840 ± 0.002	192 ± 1		2.743 ± 0.007	173 ± 4	
4 $^3T_{1u}$	2.841	194	19854	2.750	176	48013
3 $^3T_{2u}$	2.842	193	22448	2.748	176	49962
3 $^1T_{2u}$	2.841	193	23831	2.745	174	50962
5 $^3T_{1u}$	2.840	193	24078	2.747	175	51278
4 $^1T_{1u}$	2.839	191	26486	2.724	176	51567
4 $^3T_{2u}$	2.840	191	26369	2.738	162	52914
5 $^1T_{1u}$	2.834	191	30225	2.743	172	53010
3 1E_u	2.840	192	24809	2.749	176	53071
3 3E_u	2.840	192	24358	2.749	176	53163
4 $^1T_{2u}$	2.839	191	27023	2.741	170	53509
$\langle 4f^{13}6s^1 \rangle$	2.907 ± 0.001	203 ± 1		2.818 ± 0.001	175 ± 1	
6 $^3T_{1u}$	2.907	203	34817	2.818	175	61100
5 $^3T_{2u}$	2.907	203	35124	2.819	176	61308

$2\ ^3A_{2u}$	2.907	204	35200	2.820	177	61485
$6\ ^1T_{1u}$	2.906	204	35583	2.816	173	61983
$2\ ^1A_{2u}$	2.907	203	35965	2.819	175	62138
$5\ ^1T_{2u}$	2.906	203	35869	2.818	174	62195

TABLE II: Results of the calculations on the $(\text{YbBr}_6)^{4-}$ cluster that include CsCaBr₃ embedding, 80 valence electron correlation, and relativistic effects, up to spin-orbit coupling. Yb–Br bond distances, R_e , in Å; totally symmetric vibrational frequencies, $\bar{\nu}_{a_{1g}}$, in cm^{-1} ; minimum-to-minimum energy differences, T_e , relative to the $4f^{14}\text{--}1A_{1g}$ ground state, in cm^{-1} ; absorption oscillator strengths, f ; and analyses of the spin-orbit wave functions. Manifold averages and mean square deviations of the individual values with respect to the averages are labeled as $\langle 4f^{13}5d(t_{2g})^1 \rangle$, $\langle 4f^{13}5d(e_g)^1 \rangle$, and $\langle 4f^{13}6s^1 \rangle$.

state ¹	R_e	$\bar{\nu}_{a_{1g}}$	T_e	$f \times 10^2$ ²	Weights of spin-orbit free wave functions ³									
1 A_{1g}	2.732	185	0											
$\langle 4f^{13}5d(t_{2g})^1 \rangle$	2.704±0.001	186±2												
lowest, highest, and T_{1u} states of the $4f^{13}[7/2(^2F)] \times 5d(t_{2g})^1$ submanifold ¹														
1 T_{2u}	2.708	186	23890		89.98	01	$^3T_{1u}$							
1 T_{1u}	2.705	184	26555	0.273	37.59	02	$^3T_{1u}$	33.99	01	$^1T_{1u}$	11.74	01	3E_u	
					9.49	01	$^3T_{1u}$							
2 T_{1u}	2.705	184	26598	1.260	32.20	01	$^3T_{1u}$	15.20	02	$^1T_{1u}$	13.59	01	$^3T_{2u}$	
					11.76	02	$^3T_{1u}$	10.49	03	$^1T_{1u}$	6.57	01	$^1T_{1u}$	
					5.66	03	$^3T_{1u}$							
3 T_{1u}	2.705	187	27200	0.030	45.13	01	3E_u	24.15	02	$^3T_{1u}$	11.99	01	$^3T_{2u}$	
					9.17	02	$^3T_{2u}$							
4 T_{1u}	2.704	186	28355	0.000	47.20	02	3E_u	31.81	02	$^3T_{2u}$	9.42	01	$^1T_{1u}$	
5 T_{1u}	2.703	183	29072	0.084	28.23	02	$^1T_{1u}$	21.17	02	$^3T_{2u}$	15.98	03	$^1T_{1u}$	
					12.30	01	$^3T_{2u}$	8.18	01	$^3A_{1u}$	5.66	01	$^3T_{1u}$	
6 T_{1u}	2.703	186	29884	0.489	43.21	03	$^3T_{1u}$	38.70	01	$^3A_{1u}$				
2 A_{2u}	2.703	187	29992		47.59	02	$^3T_{2u}$	45.80	01	$^1A_{2u}$	6.46	01	$^3T_{2u}$	
lowest, highest, and T_{1u} states of the $4f^{13}[5/2(^2F)] \times 5d(t_{2g})^1$ submanifold ¹														
3 A_{1u}	2.707	186	34560		93.95	01	$^3T_{1u}$							
7 T_{1u}	2.707	182	35916	1.524	40.38	01	$^3T_{1u}$	29.72	03	$^1T_{1u}$	15.27	01	$^3T_{2u}$	
					8.84	01	3E_u							
8 T_{1u}	2.706	182	37503	2.304	32.16	01	$^3T_{2u}$	21.80	02	$^1T_{1u}$	19.72	03	$^1T_{1u}$	
					15.48	01	3E_u							
9 T_{1u}	2.703	184	38301	0.033	37.78	01	$^1T_{1u}$	15.61	02	$^3T_{1u}$	12.29	01	$^3T_{2u}$	

16 T_{2u}	2.816	162	57159		42.74	3 3E_u	34.93	5 $^3T_{1u}$	14.43	4 $^3T_{2u}$
5 A_{2u}	2.827	170	57293		96.16	4 $^3T_{2u}$				
17 T_{2u}	2.799	239	57355		48.41	5 $^3T_{2u}$	25.12	2 $^3A_{2u}$	19.59	6 $^3T_{1u}$
19 T_{1u}	2.792	233	57493	0.000	36.84	3 3E_u	14.40	4 $^1T_{1u}$	11.27	4 $^3T_{2u}$
					9.92	5 $^1T_{1u}$	9.84	5 $^3T_{2u}$	7.11	5 $^3T_{1u}$
					6.05	6 $^3T_{1u}$				
13 E_u	2.766	205	58110		62.80	5 $^3T_{2u}$	36.62	6 $^3T_{1u}$		
18 T_{2u}	2.761	223	58154		29.27	5 $^1T_{2u}$	25.04	2 $^3A_{2u}$	20.16	4 $^3T_{2u}$
					13.59	4 $^1T_{2u}$	9.60	6 $^3T_{1u}$		
20 T_{1u}	2.761	233	58211	0.009	49.65	6 $^1T_{1u}$	36.97	5 $^3T_{2u}$	7.36	6 $^3T_{1u}$
6 A_{2u}	2.764	203	58764		51.54	2 $^1A_{2u}$	45.05	5 $^3T_{2u}$		
19 T_{2u}	2.755	214	58932		32.22	4 $^3T_{2u}$	28.00	4 $^1T_{2u}$	19.08	5 $^1T_{2u}$
					9.72	6 $^3T_{1u}$	7.29	2 $^3A_{2u}$		

$$\langle 4f^{13}6s^1 \rangle^5 \quad 2.819 \pm 0.001 \quad 177 \pm 3$$

$4f^{13}[5/2(^2F)] \times 6s^1$ submanifold

14 E_u	2.819	175	66964		63.11	6 $^3T_{1u}$	36.84	5 $^3T_{2u}$		
20 T_{2u}	2.819	177	67051		46.52	6 $^3T_{1u}$	37.22	5 $^3T_{2u}$	11.18	2 $^3A_{2u}$
					5.02	5 $^1T_{2u}$				
21 T_{1u}	2.818	174	67353	0.027	45.86	6 $^1T_{1u}$	34.41	5 $^3T_{2u}$	19.68	6 $^3T_{1u}$
21 T_{2u}	2.818	182	67466		42.11	5 $^1T_{2u}$	31.30	2 $^3A_{2u}$	14.14	6 $^3T_{1u}$
					12.40	5 $^3T_{2u}$				
7 A_{2u}	2.819	175	67473		53.40	5 $^3T_{2u}$	46.55	2 $^1A_{2u}$		

¹ Data for the twenty $4f^{13}[7/2(^2F)] \times 5d(t_{2g})^1$ states and the fifteen $4f^{13}[5/2(^2F)] \times 5d(t_{2g})^1$ states are given in Ref. 33; only manifold averages and data relevant to this work are given here.

² Oscillator strengths for the $1A_{1g} \rightarrow iT_{1u}$ absorptions were calculated at the ground state equilibrium distance: 2.732 Å.

³ Weights (in %) larger than 5% are given. They have been calculated at $R(\text{Yb-Br})=2.705$ Å.

⁴ Only states of the $4f^{13}[7/2(^2F)] \times 5d(e_g)^1$ submanifold are included in the average.

⁵ Only states of the $4f^{13}[5/2(^2F)] \times 6s^1$ submanifold are included in the average.

TABLE III: Data of potentially emitting levels and characteristics of the predicted emissions. Energies are given in cm^{-1} .

	level	spin character	energy gap	p ^a	emission characteristics	emission energy calculated	emission energy observed ^b
$4f^{13}(7/2)5d(t_{2g})^1$	$1T_{2u}, 1E_u$	high	23900	128	spin-forbidden, slow	23900	23000
	$1T_{1u}, 2T_{1u}$	mixed	2600	13	spin-enabled, 400 <i>ns</i>	26600	24500
$4f^{13}(5/2)5d(t_{2g})^1$	$3A_{1u}$	high	4600	24	spin-forbidden, slow	34600	
$4f^{13}(7/2)5d(e_g)^1$	$8E_u$	high	4000	22	spin-forbidden, slow	43900	
$4f^{13}(5/2)5d(e_g)^1$	$6A_{1u}$	high	5200	30	not observable (in CB)	53900	

^aMultiphonon order, $p = E_{gap}(i\Gamma)/\hbar\nu_{max}$. See text for details.

^bPeak position approximately read from the 77 K emission spectrum of Ref. 3.

FIG. 1: Breathing mode potential energy curves of the $4f^{14}$, $4f^{13}5d^1$, and $4f^{13}6s^1$ manifolds of $\text{CsCaBr}_3:(\text{YbBr}_6)^{4-}$. All results include embedding and scalar relativistic effects. Left: spin-orbit free CASSCF($4f,5d,6s$) calculations; Right: spin-orbit free MS-CASPT2(Br48,Yb32) calculations. See text for details.

FIG. 2: Breathing mode potential energy curves of the $4f^{13}5d^1$ and $4f^{13}6s^1$ manifolds of $\text{CsCaBr}_3:(\text{YbBr}_6)^{4-}$. All results include embedding, scalar relativistic effects, and dynamic electron correlation of 80 valence electrons. Left: spin-orbit free MS-CASPT2(Br48,Yb32) calculations; Right: spin-orbit CI calculations. Spin-orbit splitting of the manifolds in the left, leading to submanifolds in the right is indicated with arrows. The submanifolds are labeled by the effective J value of their $4f^{13}$ subshell. See text for details.

FIG. 3: Calculated absorption spectrum of $\text{CsCaBr}_3:(\text{YbBr}_6)^{4-}$ using spin-orbit CI data from Table II and different values for the line broadening parameter (40 and 5 cm^{-1} in the low and high resolution spectra, respectively). The fourteen most intense T_{1u} electronic origins are indicated with the ordinals used in Table II. Electric dipole forbidden transitions are indicated with vertical bars.

FIG. 4: First two bands of the calculated emission spectrum of $\text{CsCaBr}_3:(\text{YbBr}_6)^{4-}$ using spin-orbit CI data from Table II and different values for the line broadening parameter (40 and 5 cm^{-1} in the low and high resolution spectra, respectively). The electric dipole forbidden emissions are indicated with vertical bars.

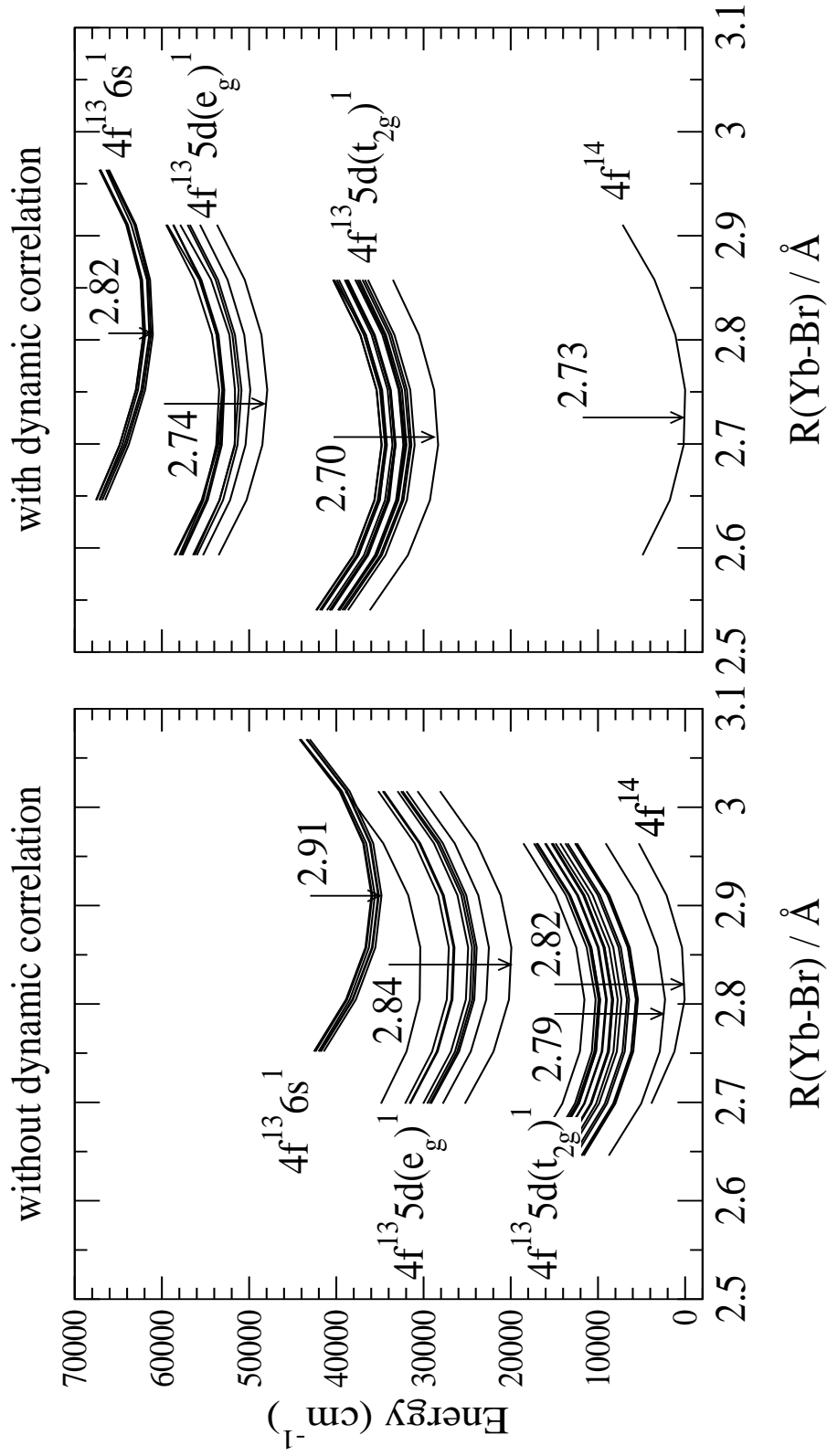


Figure 1. Sánchez-Sanz *et al.*

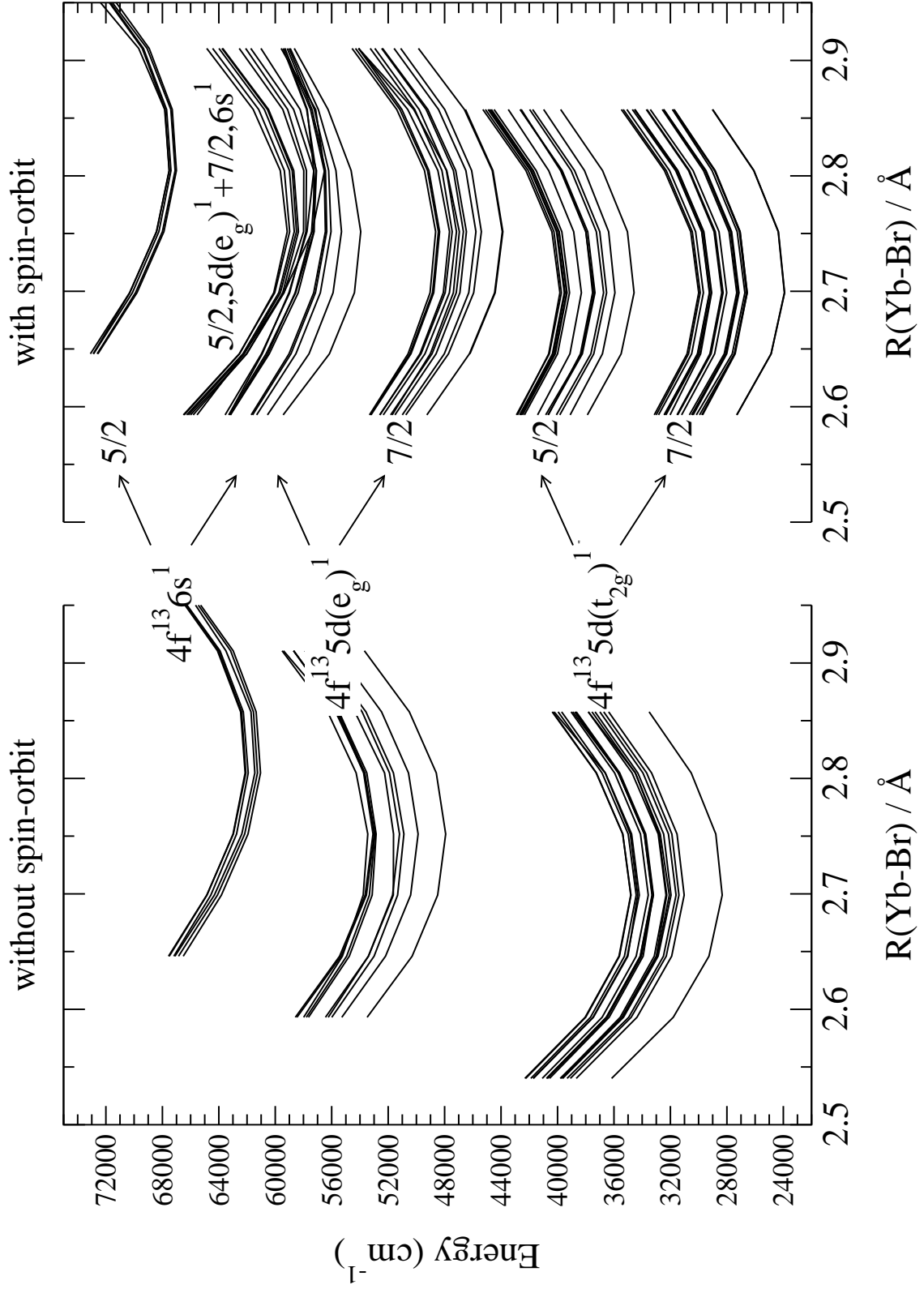


Figure 2. Sánchez-Sanz *et al.*

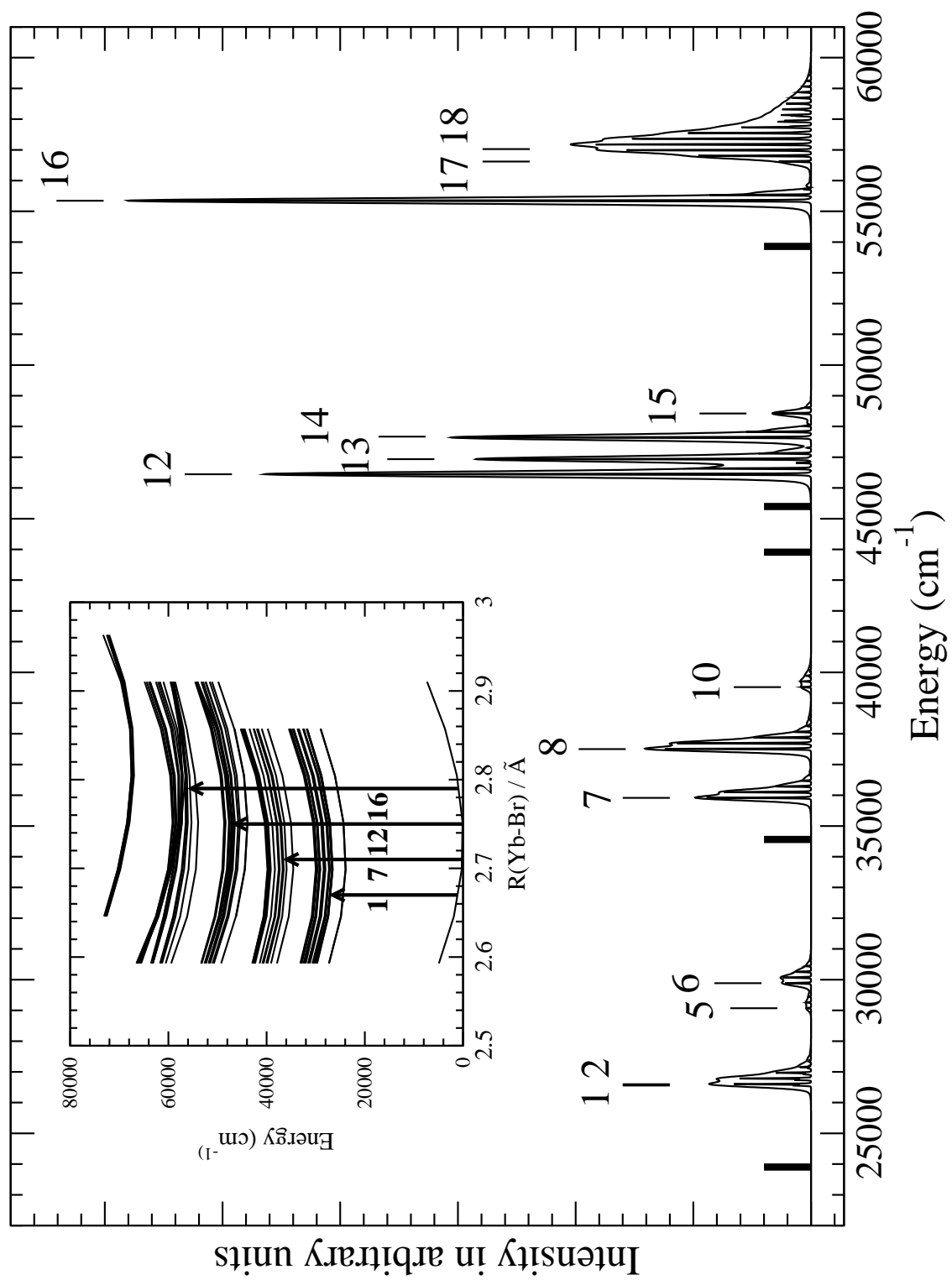


Figure 3. Sánchez-Sanz *et al.*

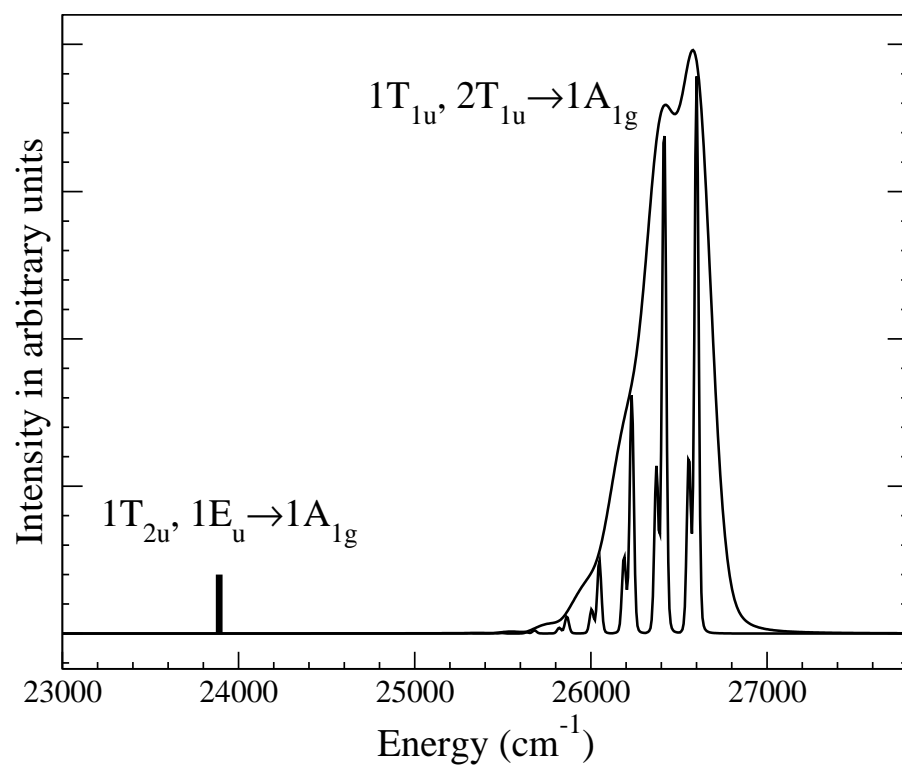


Figure 4. Sánchez-Sanz *et al.*